Safe Flight Using One Aerodynamic Control Surface

Raghu Venkataraman* and Peter Seiler†
Department of Aerospace Engineering & Mechanics
University of Minnesota, Minneapolis, MN, 55455, USA

Civil unmanned aircraft will need to meet stringent safety standards before they are certified to operate in the national airspace of the United States. Reliability is a key requirement for certification. Most current civil unmanned aircraft are not reliable because of the presence of single points-of-failure and the use of low-reliability components. For example: Many fixed-wing unmanned aircraft are equipped with only two aerodynamic control surfaces. A fault in any one surface will usually spell catastrophe. This paper demonstrates how this single point-of-failure can be removed using multi-variable control laws. A single aerodynamic control surface is shown to be sufficient to stabilize the aircraft and execute a set of limited maneuvers. These limited maneuvers are sufficient to safely fly to a landing spot. This concept is proved using flight tests on an unmanned aircraft at the University of Minnesota. The results are also applicable to manned commercial aircraft. Controllability with one surface indicates the large potential to mitigate faults that might otherwise lead to loss-of-control events.

I. Introduction

Recently, unmanned aerial vehicles/systems (UAVs/UASs) have found increasing civilian and commercial applications, such as law enforcement, search and rescue, and precision agriculture. These commercial applications require UAVs to operate in civilian airspace. Central to operating UAVs in civilian airspace is the challenge of meeting the stringent safety standards set by the Federal Aviation Administration (FAA). In 2012, the United States Congress passed H.R.658[1] - the FAA Modernization and Reform Act - in order to facilitate the safe integration of UASs into the national airspace. In particular, section 332 of H.R.658 mandates the FAA to "provide for the safe integration of civil unmanned aircraft systems into the national airspace system as soon as practicable, but not later than September 30, 2015." More recently, the FAA released the Notice of Proposed Rulemaking.[2] This is thought to be the precursor to the impending release of detailed policy. This brings in legislative and policy dimensions to what is academically seen as a technical challenge.

To put this challenge in perspective, consider the current safety standards set by the FAA for manned commercial aircraft. In order for a manned commercial aircraft to be certified, there should be no more than one catastrophic failure per 10^9 flight hours. Commercial aircraft manufacturers, such as Boeing, meet the 10^{-9} failures-per-flight-hour standard by utilizing hardware redundancy. For example, the Boeing 777 has 14 spoilers each with its own actuator; two actuators each for the outboard ailerons, left & right elevators, and flaperons; and three actuators for the single rudder.[3] On the other hand, most civil UAVs have reliabilities that are orders of magnitude below 10^{-9}. For instance, the UAV Research Group at the University of Minnesota (UMN)[4] operates an *Ultra Stick 120* aircraft (described further in section II.B) with single-string, off-the-shelf components. A comprehensive fault tree analysis yielded a failure rate of 2.2×10^{-2} failures-per-flight-hour [a] for this aircraft.[5]

UAVs have such low reliability for two main reasons. First, most on-board components are not very reliable because they are low-cost. Second, most on-board components have little to no hardware redundancy. Consequently, there are single points of failure that can lead to catastrophic failure. Safe integration of

*Graduate Student, venka085@umn.edu
†Assistant Professor, seile017@umn.edu
[a]This analysis provides a theoretical estimate of the reliability and no loss of aircraft has occurred to date.

Figure 1. Sentera Vireo[6] - a two-surface UAV.

UAVs into the national airspace requires increases in UAV reliability. However, the solutions adopted to increase the reliability of manned commercial aircraft are not downwardly scalable to UAVs. In particular, hardware redundancy must be used judiciously because of the costs associated with size, weight, and power. Analytically redundant solutions, such as robust and fault-tolerant control, have the potential to bridge the gap between commercial aircraft, that almost entirely use hardware redundancy, and current UAVs, that are almost entirely single-string designs. Irrespective of the aircraft type, one key technical challenge in aircraft reliability is introducing tolerance to faults in the aerodynamic control surfaces. A common strategy for tolerating a faulty control surface is the reallocation of the remaining functional control surfaces. However, the worst-case scenario is when the aircraft is down to its last functional control surface and there are no remaining surfaces that can be reallocated.

The problem of controlling an aircraft with only one control surface is motivated by the increasing popularity of small UAVs that are equipped with only two control surfaces. Examples of such two-surface UAVs include the Sentera Vireo,[6] Agribotix Hornet,[7] Trimble UX5,[8] and senseFly eBee.[9] In all four examples, a pair of elevons provide roll and pitch control authorities. If the aircraft is not fault-tolerant, both elevons are safety-critical. In other words, without advanced feedback control laws, a fault in any one surface will eventually lead to loss of control (LOC) and catastrophic failure. This paper demonstrates that an aircraft can be safely flown with only one functional aerodynamic control surface. An immediate implication of this result is that the two-surface UAVs, introduced above, can be made fault-tolerant up to one control surface. Specifically, single-surface fault-tolerance is provided by robust, multivariable feedback control laws.

It should be emphasized that the use of all aerodynamic control surfaces is still necessary for maximizing flight performance. Flight with one control surface comes with the cost of degraded command tracking performance. However, one control surface is sufficient for the aircraft to safely fly home, as explained in section II.A. Two specific multivariable control synthesis techniques (linear quadratic Gaussian (LQG) and H_∞) are described in section III. The resulting control laws are tested on an example UAV, described in section II.B. Flight test results, presented in section IV, demonstrate the proof of concept.

The focus of this paper is on fixed-wing unmanned aircraft, but the results are qualitatively applicable to fixed-wing manned aircraft as well. As an example, consider the Boeing 777. The result presented in this paper suggests that it should be possible to fly a 777, with limited maneuverability, with only one control surface. Of course, not all control surfaces on the 777 qualify for this challenge. Only control surfaces that have sufficiently high roll and pitch control authorities, such as the left elevator, can provide full controllability. Given the triple-triple hardware redundancy of the 777, it may be argued that the likelihood of a scenario where there is only one functional control surface is extremely small. Even if such a scenario is statistically insignificant, the result presented in this paper is still relevant to manned commercial aircraft. In particular, it demonstrates that commercial manned aircraft have a large potential to use fault-tolerant control for mitigating faults that might otherwise lead to loss-of-control events.

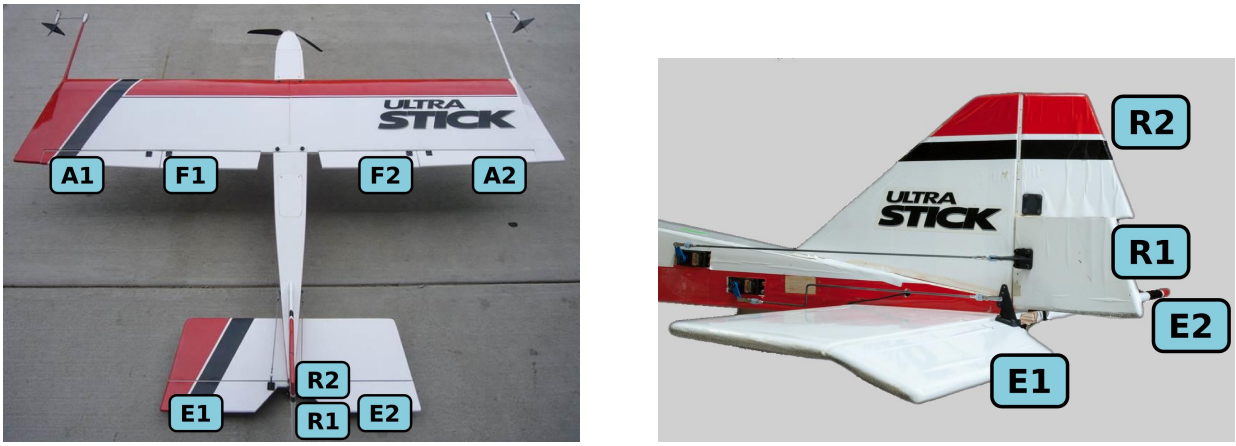

(a) Top view

(b) Empennage with split surfaces

Figure 2. Ultra Stick 120 "Baldr" - the technology demonstrator

II. Problem Formulation

II.A. Objective

The main result of this paper is demonstrating the possibility of safely flying a fixed-wing aircraft with only one aerodynamic control surface. To motivate this result, consider a typical two-surface UAV such as the Sentera Vireo, pictured in figure 1. The Vireo has a pair of elevons that provide roll and pitch control authorities. Normally, both elevons are mission-critical. In other words, a failure in either elevon leads to loss of mission (LOM). However, if the aircraft is not fault-tolerant, both elevons become safety-critical. A safety-critical component is one whose failure eventually leads to catastrophic failure. In addition to being safety-critical, the two elevons are also *individual* single-points-of-failure on the Vireo. In other words, a single failure in either elevon is all it takes to cause catastrophic failure. This paper shows how advanced feedback control techniques can be used to make two-surface UAVs tolerant to faults in either surface.

All the two-surface UAVs introduced in section I are used for aerial surveillance and mapping. After a control surface failure, the mission is degraded to *safely flying home*. In order to safely fly home, the aircraft should be able to execute a limited set of maneuvers. This includes, at the very least, straight and level flight at constant altitude, either left or right banked turns, and steady descents. It is reasonable to suggest that a flight path to a safe landing spot can be generated using combinations of these canonical maneuvers. Based on this premise, the problem of safely flying home is instead simplified to executing the limited set of maneuvers. The results presented in section IV will demonstrate the execution of these canonical maneuvers.

II.B. Technology demonstration platform

The technology demonstrator is a small UAV, named Baldr, that is maintained and operated by UMN's UAV Research Group. Baldr is based on the Ultra Stick 120 airframe, and is pictured in figures 2(a) and 2(b). The Ultra Stick 120[10] is a commercial, off-the-shelf, radio-controlled aircraft with a wingspan of 1.92m and a mass of about 8kg. The UMN UAV Research Group has retrofitted the airframe with custom avionics for enabling research in the areas of real-time control, guidance, navigation, and fault detection. The avionics include a sensor suite, a flight control computer, and a telemetry radio.[4, 11, 12]

Baldr has a total of eight aerodynamic control surfaces, each actuated by its own servo motor. These surfaces are labeled in figures 2(a) and 2(b) as flaps ($F_{1,2}$), ailerons ($A_{1,2}$), elevators ($E_{1,2}$), and rudders ($R_{1,2}$). The split elevators and rudders are custom modifications that are unique to Baldr. The sign convention of the control surfaces is as follows. A trailing edge down deflection of the elevators, ailerons, and flaps is considered positive. A trailing edge left deflection of the rudders, when the aircraft is viewed top-down with the nose pointing forward, is considered positive. In addition, all the surfaces have a deflection range of $[-25°, +25°]$. While each surface is independently actuated, the flight software allows for them to be coupled symmetrically (such as the elevators) or anti-symmetrically (such as the ailerons). While Baldr may appear to be over-actuated for a small UAV, the flight software allows the control designer to choose the specific surfaces that are to be controlled. Moreover, these redundant surfaces allow for the testing and

validation of fault-tolerant and reconfigurable control laws. This is precisely why this aircraft is chosen as the technology demonstrator in this research. From an infrastructure standpoint, this aircraft serves as the test platform for all the safety-critical and aircraft reliability research that is being undertaken by the UMN UAV Research Group.

A high-fidelity simulation environment for the Ultra Stick 120 is publicly available.[4] This simulation environment was built using Matlab/Simulink and contains models for the aircraft subsystems. The rigid body dynamics are implemented using the standard six degree-of-freedom, nonlinear aircraft equations of motion.[13] The aerodynamic stability and control derivatives were identified from wind tunnel experiments.[14,15] The simulation models the forces & moments and the propwash generated by the electric motor and propeller pair. The simulation also includes actuator models for the servo motors and sensor models for the inertial measurement unit (IMU), air data probes, and magnetometer. Environmental effects, such as wind gusts, atmospheric turbulence, and the Earth's gravitational & magnetic fields are modeled using subsystems. The nonlinear aircraft model can be trimmed and linearized at any flight condition within the flight envelope of the aircraft. The simulation environment and the flight control computer allow for extensive software-in-the-loop and hardware-in-the-loop simulations. The entire simulation environment, details about the aircraft fleet, components, wiring, and data from numerous flight tests have been made open-access and can be freely downloaded from.[4]

II.C. Scope of demonstration

Experimental flight tests are conducted on the Baldr UAV to demonstrate safe flight using only one control surface. Since Baldr is equipped with eight control surfaces, the flight computer is used to select the single surface to be actuated. This single surface must have sufficiently high roll and pitch control authorities. The only surfaces that qualify for this challenge are the left and right elevators (E_1 and E_2 in figure 2(b)). The ailerons, flaps, and rudders have negligible pitch control authority. Baldr is representative of conventional airframes with a fuselage and empennage. In addition, by employing the split elevators as elevons, Baldr can also act like a two-surface UAV. Therefore, demonstrating safe flight on Baldr with only the left or right elevator should be a good indicator of whether the same is possible on larger conventional aircraft as well as on smaller two-surface UAVs.

Irrespective of the type of aircraft that is being emulated, a baseline control law is used when all surfaces are healthy. A realistic implementation of fault-tolerant control will include a fault detection and isolation (FDI) algorithm, a backup control law, and a transition scheme to switch between the baseline and backup control laws. A FDI algorithm for detecting and isolating faults in the split rudders of Baldr is discussed in.[16] This FDI algorithm and many others that are discussed in literature[17,18,19] can be suitably adapted for the split elevators of Baldr. In this paper, a FDI algorithm is assumed to be available and the focus is on the backup control law. The transition scheme is a simple instantaneous switch from the baseline to the backup control law.

The results presented in this paper are limited by the scope of failure modes covered, in two specific ways. First, only instantaneous stuck actuator faults are considered. This assumption disregards dynamic actuator fault modes, such as oscillatory and ramp failures. Second, the actuators are assumed to get stuck at their respective trim positions. In other words, only fault modes that do not alter the trim point are considered. While these two assumptions may seem overly restrictive, it is a good starting point for a technology demonstration exercise. In order to make this scope rigorous and set the stage for control design (section III), some mathematical preliminaries are introduced below.

II.D. Mathematical preliminaries

The aircraft equations of motion[20] can be described in the nonlinear state-space form, as shown in equations 1 and 2.

$$\dot{x} = f(x, u, t) \tag{1}$$

$$y = h(x, u, t) \tag{2}$$

In this form, $x \in \mathbb{R}^n$ is the state vector, $u \in \mathbb{R}^m$ is the input vector, $y \in \mathbb{R}^p$ is the output vector, and $t \in \mathbb{R}^+$ is time. In addition, $f : \mathbb{R}^n \times \mathbb{R}^m \times \mathbb{R}^+ \to \mathbb{R}^n$ is the state function and $h : \mathbb{R}^n \times \mathbb{R}^m \times \mathbb{R}^+ \to \mathbb{R}^p$ is the output function. The state vector is: $x = [\phi, \theta, p, q, r, u, v, w]^T$. Here, ϕ and θ are two of the Euler

angles of the aircraft. The third Euler angle (ψ), is not included in the state vector because only inner loop controllers are developed in this paper. The aircraft's angular velocity in the body-fixed frame are: roll rate (p), pitch rate (q), and yaw rate (r). The airspeed components in the body-fixed frame are u, v, and w. It was mentioned in section II.C that only the left and right elevators qualify for the challenge of single surface flight. Consequently, the input vector is: $u = [\tau, E_1, E_2]^T$. Here, τ is the throttle setting and E_1 and E_2 are the deflections of the left and right elevators, respectively. The airspeed, angle of attack, angle of sideslip, and flight path angle are denoted by V, α, β, and γ, respectively.

Aircraft typically fly around equilibrium or trim points. These are operating points at which some state derivatives are zero, and others have constant values. The collection of all such trim points defines the steady flight envelope ($\mathbb{F}$) of the aircraft, as shown in equation 3.

$$\mathbb{F} = \{(\bar{x}, \bar{u}) : f(\bar{x}, \bar{u}) = 0\} \tag{3}$$

The limited set of maneuvers described in section II.A can be described as subsets of $\mathbb{F}$, as given in equations 4 through 6. Banked right turns have a form similar to equation 6, except that $\bar{\phi} > 0$.

$$\mathbb{F}_{straight,level} = \{(\bar{x}, \bar{u}) \in \mathbb{F} : \bar{p} = \bar{q} = \bar{r} = \bar{\phi} = \bar{\gamma} = 0\} \tag{4}$$

$$\mathbb{F}_{steady,descent} = \{(\bar{x}, \bar{u}) \in \mathbb{F} : \bar{p} = \bar{q} = \bar{r} = \bar{\phi} = 0,\ \bar{\gamma} < 0\} \tag{5}$$

$$\mathbb{F}_{banked,left} = \{(\bar{x}, \bar{u}) \in \mathbb{F} : \bar{\phi} < 0,\ \bar{\gamma} = 0\} \tag{6}$$

The scope of demonstration (section II.C) can now be mathematically defined. Consider, for example, a stuck fault in the right elevator (E_2) that occurs at time T_f. Moreover, let the trim deflection be $\bar{E}_2$. The assumptions of section II.C imply that $E_2(t \geq T_f) \equiv \bar{E}_2$. When the same assumption is applied to all the stuck surfaces, it is seen that the trim point $(\bar{x}, \bar{u})$ is unaltered by the control surface faults. This simplification serves well to demonstrate the proof of concept in this paper. In particular, the steady-state of the aircraft is unaltered, implying that the actuator faults induce small transients in the aircraft states. These small transients make the switchover from the baseline to the backup control law smooth and stable. However, it is acknowledged that a rigorous demonstration will involve relaxing these assumptions to include dynamic actuator faults as well as trim point variations. The main impact of relaxing these assumptions will be larger transient effects in the aircraft states after the onset of the faults. These transient effects will have to be effectively managed by the backup controller. Controllers that have enhanced robustness and those that explicitly depend on the operating point, such as linear parameter varying (LPV) controllers, are promising solutions.

III. Fault-Tolerant Control Synthesis

III.A. Linear aircraft model

The nonlinear aircraft model is linearized about the nominal trim point (see appendix A) for applying linear control synthesis techniques. The linearized aircraft model has a state-space representation shown in equations 7 and 8.

$$\dot{\tilde{x}} = A\tilde{x} + B\tilde{u} \tag{7}$$

$$\tilde{y} = C\tilde{x} + D\tilde{u} \tag{8}$$

The linearized dynamics are written in terms of the perturbation quantities: $\tilde{x}$, $\tilde{u}$, and $\tilde{y}$. The total signal is the sum of the trim and perturbation components. For example, $x = \bar{x} + \tilde{x}$. Throughout the remainder of this section, the tilde will be dropped from the perturbation components of the linear model.

For demonstration, the left elevator is the only controllable surface. The corresponding input vector is $u = E_1$. It should be noted that, in general, the throttle can also be used for fault-tolerant control. However, this is not investigated in this paper. The state vector is the same as before: $x = [\phi, \theta, p, q, r, u, v, w]^T$. The output vector is $y = [\phi, \theta, p, q, r]$, and contains all the measured and estimated signals used for feedback control. The angular rates in the body-fixed frame (p, q, r) are directly measured by Baldr's strapdown IMU - the only sensor that is used for feedback control in this paper. The Euler angles (ϕ, θ) are estimated using

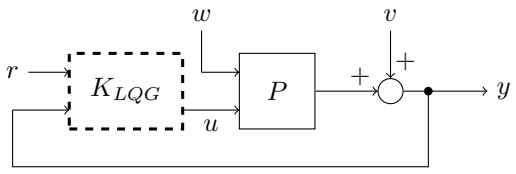

Figure 3. Linear Quadratic Gaussian control law

a fifteen-state extended Kalman filter (EKF).[12] The linear accelerations (ax, ay, az) from the strapdown IMU are not used in feedback because of the presence of biases. Although these biases can be easily estimated using the EKF, this is not done in this paper for the sake of simplicity. Given this output vector, only inner loop controllers are developed. The nominal trim point of Baldr and the linear aircraft model are given in appendix A. This linear model can be shown to be both controllable and observable using the Kalman rank test. In addition, a balanced realization of P has the following Hankel singular values: $[9.44, 4.93, 3.4, 1.72, 0.59, 0.06, 0.02, 0.02]$. Although the Hankel singular values indicate that some states are more controllable and observable than others, the full order model is used for control synthesis.

The baseline control law for Baldr is a classical loop-at-a-time design. In this design, the longitudinal and lateral-directional aircraft dynamics are assumed to be decoupled. Hence, separate loops are designed for each dynamics. The longitudinal loop controls the throttle and elevators. The lateral-directional loop controls the ailerons and rudders. Flaps are pilot-controlled. Each control loop has a classical cascade structure with inner and outer loops. More details about the baseline control law can be found in.[11] The backup control laws are synthesized using multi-variable control theory[21] and are based on the linear model given in appendix A. The backup control laws are designed to actuate only the left elevator (E_1) while locking all the remaining surfaces into their respective trim positions. A multi-input-multi-output (MIMO) approach is necessary for synthesizing the backup control laws because the left elevator excites both the longitudinal and the lateral-directional dynamics.

III.B. Linear quadratic Gaussian control

The first backup control law is a linear quadratic Gaussian (LQG) design, shown by the dashed box K_{LQG} in figure 3. LQG controllers are primarily used for output regulation around the trim point. However, in order to demonstrate command tracking, integrators can be added to specific output channels. In this paper, the LQG control law regulates p, q, r around zero and tracks roll and pitch reference commands. The controller K_{LQG} has a two degrees-of-freedom structure: one for the reference commands r and the other for the measurements y. The LQG controller has three parts internally (not shown in figure 3): a total feedback gain, a Kalman filter, and integrators. The total feedback gain is composed of the optimal state feedback gain (K_{sf}) as well as the integral gain. The state feedback gain has a size compatible with the state vector.

The state feedback law $u = -K_{sf}\hat{x}$ minimizes the following quadratic cost function,

$$J(x_0, u) = \int_0^\infty \left(\hat{x}^T Q \hat{x} + u^T R u\right) dt, \tag{9}$$

subject to the system dynamics given in equation 7. In equation, 9, $\hat{x}$ is the estimated state vector and x_0 is the initial condition at $t = 0$. The state feedback gain K_{sf} is obtained by solving an associated algebraic Riccati equation.[21] A Kalman filter is used to provide the state estimates $(\hat{x})$ to the state feedback law. The Kalman filter has access to sensor measurements (y) and control commands (u). The Kalman filter minimizes the steady-state covariance of the error in the state estimates: $\lim_{t\to\infty} E\left[(x - \hat{x})\,(x - \hat{x})^T\right]$. Figure 3 also shows process noise (w) and measurement noise (v) signals. The covariance of these signals are used in the synthesis of the Kalman filter.

K_{LQG} also contains integrators for tracking roll and pitch reference commands, supplied as: $r = [\phi_{cmd}, \theta_{cmd}]^T$. The tracking error (e) is formed between r and the estimated Euler angles as: $e = r - [\phi, \theta]^T$. The tracking error is integrated over time and then multiplied by the integral gain. The values of the parameters used in the LQG synthesis are given in appendix B. The LQG control law has limited objectives: regulating p, q, r around zero and tracking ϕ_{cmd} and θ_{cmd}. In order to incorporate multiple control objectives and enhance the disturbance rejection properties of the closed loop, H_∞control is investigated next.

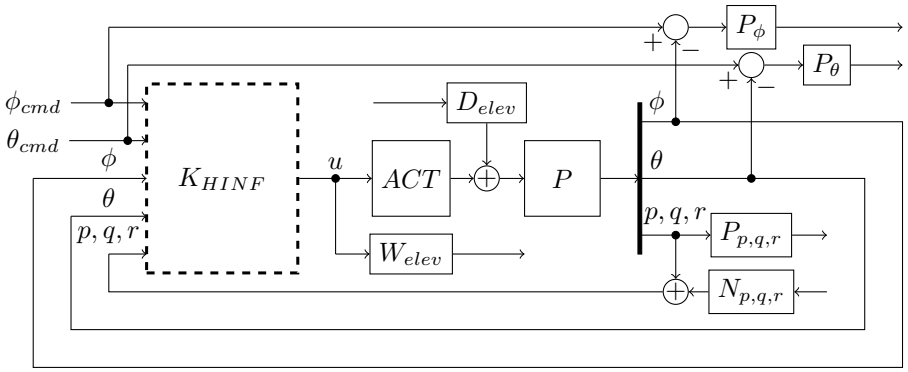

Figure 4. H_∞control law - generalized plant interconnection

Table 1. Closed-loop robustness properties

Property	LQG closed loop	H_∞closed loop
Input sensitivity $\|S_i\|_\infty$	1.64 dB	3.33 dB
Output sensitivity $\|S_o\|_\infty$	5.52 dB	22.07 dB
$\|PS_i\|_\infty$	12.64 dB	10.01 dB
$\|CS_o\|_\infty$	-8.76 dB	17.57 dB
MIMO gain margin	$[0.61, 1.65]$	$[0.47, 2.11]$
MIMO phase margin	$\pm 27.56°$	$\pm 39.35°$
Critical frequency	0.24 rad/s	3.17 rad/s

III.C. H_∞control

The second backup control law is an H_∞design that allows for multiple design objectives to be specified. The generalized plant with all the weighting functions is shown in figure 4. The two degrees-of-freedom controller that is synthesized is shown by the dashed box K_{HINF}. Reference commands are ϕ_{cmd} and θ_{cmd}. Command tracking is specified by the performance weights P_ϕ and P_θ. Good command tracking performance is required at low frequencies and may be relaxed at higher frequencies. Consequently, P_ϕ and P_θ are low-pass filters. The angular rates are condensed into a vector signal labeled p, q, r. The performance weights $P_{p,q,r}$ are constant scalars and uniformly limit the angular rates of the aircraft across frequency. IMU measurement noise is incorporated into the H_∞synthesis by the output-additive weights $N_{p,q,r}$. The effect of atmospheric turbulence is modeled by the weight D_{elev} and is applied additively at the plant input. The weight W_{elev} is shaped like a high-pass filter in order to penalize high frequency control commands. This helps in limiting the bandwidth of the controller. The block ACT is a low-pass filter that models the actuator dynamics. The weighting functions were designed using insights from flight dynamics as well as past flight tests conducted on the NASA AirSTAR.[22] All weights are given in the form of transfer functions in appendix C.

III.D. Robustness analysis

The LQG and H_∞syntheses result in stable controllers that can be connected with the plant to form the closed loop. The γ value returned from the H_∞synthesis is 10.85. Table 1 lists the robustness properties of the closed loops formed with both syntheses. The plant is denoted P and the controller is denoted C. Although the peak gains of S_i and S_o are higher for the H_∞closed loop, the MIMO gain and phase margins indicate that the H_∞closed loop is more robust.

IV. Results

Flight tests of Baldr were conducted at the University of Minnesota Outreach, Research, and Education Park over three days between January, 2015 and May, 2015. Each day of the flight test witnessed different wind and turbulence conditions. The control laws described in the previous section were developed in Mat-

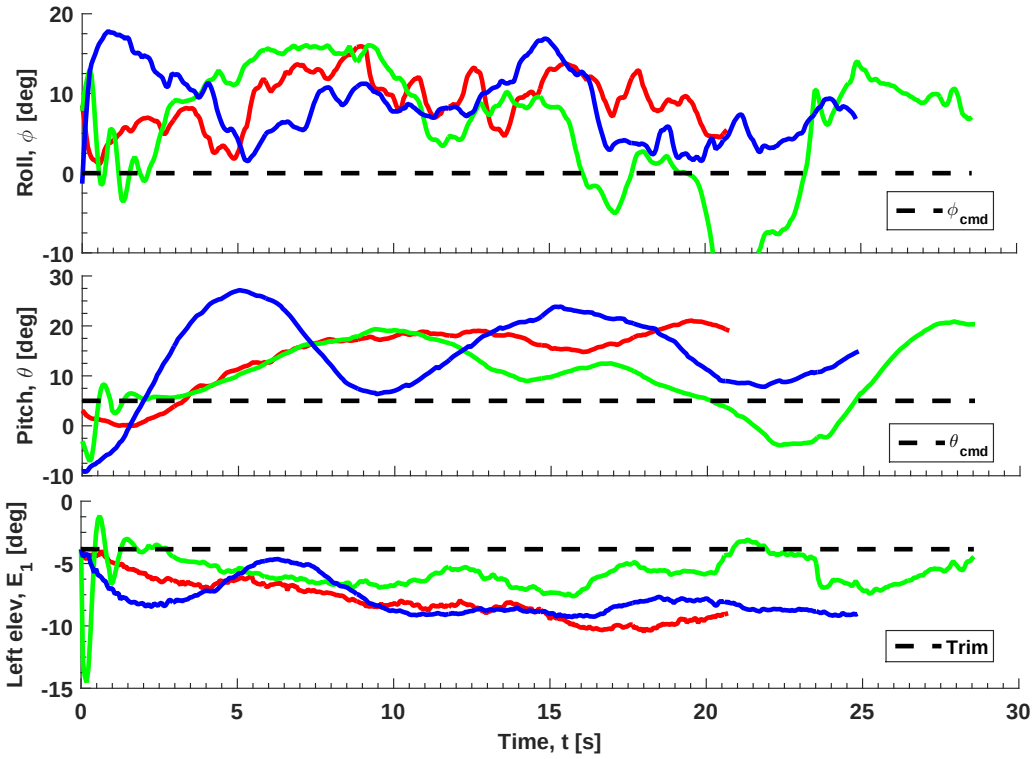

Figure 5. Flight test: LQG controller: straight and level flight (3 flights)

lab/Simulink and subsequently converted to C code using Simulink Coder. The control laws are implemented on the flight computer of Baldr at a sampling rate of 50 Hz.[4] In this section, flight test results are presented that demonstrate safe flight using only the left elevator (E_1) of Baldr. Similar conclusions automatically follow for the right elevator (E_2) due to the longitudinal symmetry of the aircraft. Of the limited set of maneuvers introduced in section II.A, only straight and level flight and banked turns at constant altitude are presented. Steady descents can be executed by decreasing the throttle, and are not shown in this paper.

IV.A. LQG flight tests

The first set of results are for the LQG control law described in section III.B. Figure 5 shows Baldr flights where the aircraft was commanded to fly straight and level at constant altitude. Figure 5 is divided into three subplots, all of which share a common time axis. The time histories of the roll angle, pitch angle, and left elevator command are shown in three different subplots. Each subplot contains data from three different Baldr flights, each shown in a different color. The red, green, and blue plots have different end times because the three flights were of different durations. The longest flight lasted 29s and is shown in green. The shortest flight lasted 21s and is shown in red. In addition, each of the three subplots contains a black dashed line. For the roll and pitch angle plots, the black dashed line represents reference commands: ϕ_{cmd} and θ_{cmd}, respectively. For the left elevator command, the black dashed line represents the trim deflection.

The first, and most important, observation from figure 5 is that the aircraft is still controllable with a single aerodynamic control surface. Both ϕ and θ appear to be under control and well within their respective flight envelope bounds. Moreover, ϕ is between 0 and 20°, with a mean of around 5°, indicating a tendency for the aircraft to roll rightwards. The only exception to this trend is the sudden left bank in the green plot near $t = 20$s. This is due to a wind gust hitting the aircraft. The effects of sensor noise and atmospheric turbulence can be seen in the high frequency content of ϕ. The low frequency variation in ϕ is more pronounced than usual, given that the aircraft is being commanded to fly straight and level.

The time response of θ, in figure 5, is degraded to a similar extent. Specifically, θ varies between 0 and 30°, with a trim value of 5°. Under the control of a single surface, the aircraft has a tendency to pitch upwards. This positive pitch deflection is seen in the red, green, and blue plots. The left elevator deflection command is shown in the bottom subplot of figure 5. The trim deflection is $\bar{E}_1 = -4°$. In all three flights,

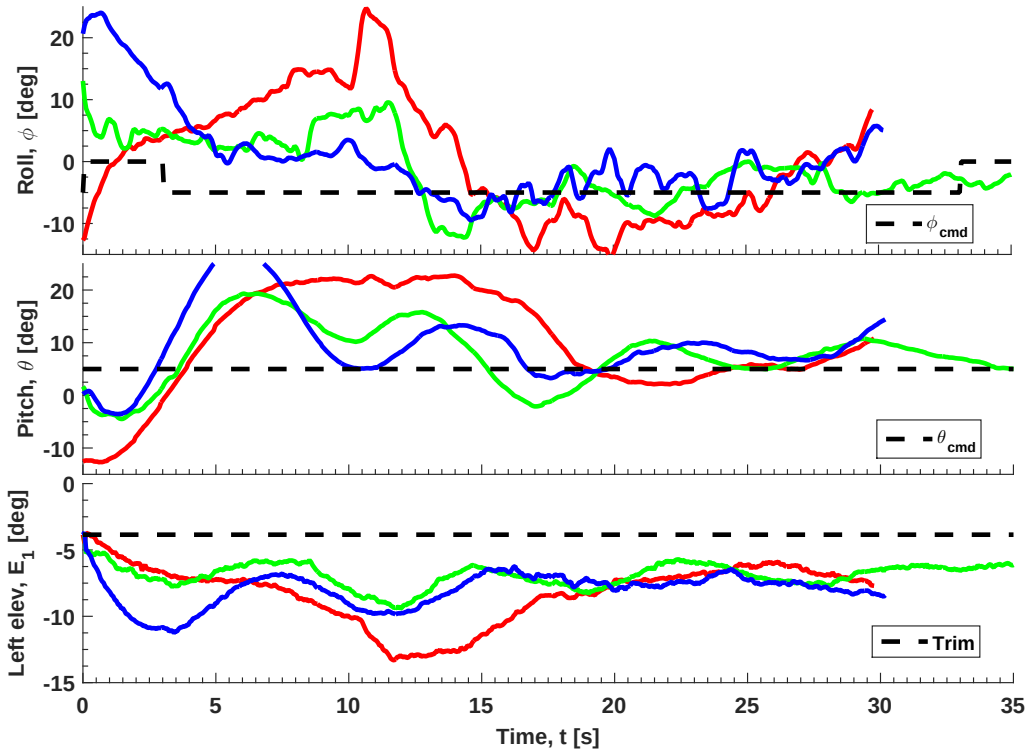

Figure 6. Flight test: LQG controller: left banked turn (3 flights)

the left elevator is commanded to deflect negatively. The variation in E_1 is largely between $-10°$ and $\bar{E_1}$, indicating that the left elevator never hits the saturation limits of $\pm 25°$.

The flight test results of Baldr performing left banked turns are shown in figure 6. Figure 6 is divided into three subplots, each showing the time history of ϕ, θ, and E_1. The red, green, and blue plots represent three different flights of Baldr executing left banked turns. The longest flight lasts 35s and is shown in green. Baldr enters into a left banked turn after a time delay of 3s and stays in this turn for a total duration of 30s. The corresponding bank angle command is $-5°$, and is shown in the plot of ϕ_{cmd}. The pitch angle command is $5°$ and is unaltered from trim. As noted previously, the most significant observation from figure 6 is that Baldr is stable and controllable while executing left banked turns with one control surface. From figure 6, it is evident that the tracking performance is better while executing left banked turns than while flying straight and level.

In particular, the ϕ response shown in figure 6 varies between $-10°$ and $20°$. For the first 10s after the start of the maneuver, ϕ is approximately between 0 and $10°$ and does not track ϕ_{cmd} well. However, 10s into the start of the maneuver, ϕ starts tracking the command well. This delayed tracking is due to the integrators added to the LQG synthesis. Subsequent variations in ϕ are within a $\pm 5°$ window centered at $\phi_{cmd} = -5°$. This is considered good tracking, especially for an aircraft flying with a single control surface. Similar observations can be made for the response of θ. The θ tracking performance is poor immediately after the start of the maneuver. However, the integral action in the control law kicks in and θ starts to track θ_{cmd} around the $t = 20$s mark. Subsequent variations in θ are also within a $\pm 5°$ window centered at the trim value of $5°$. The left elevator deflection command is between $-15°$ and the trim value of $-4°$. In all three flights, the left elevator is commanded to deflect negatively. This is consistent with the expected surface deflection for executing left banked turns.

In summary, the results of this section prove that Baldr is stable and controllable even when only one aerodynamic control surface is available. Successful flight tests were also conducted for Baldr performing right banked turns. This case is similar to left banked turns and the corresponding data is not presented here due to space constraints. The LQG control law of section III.B performs satisfactorily in flight. All state variables stay within, and do not depart from, their respective flight envelope bounds. While the overall tracking performance is certainly degraded, this is the cost associated with flying a handicapped aircraft.

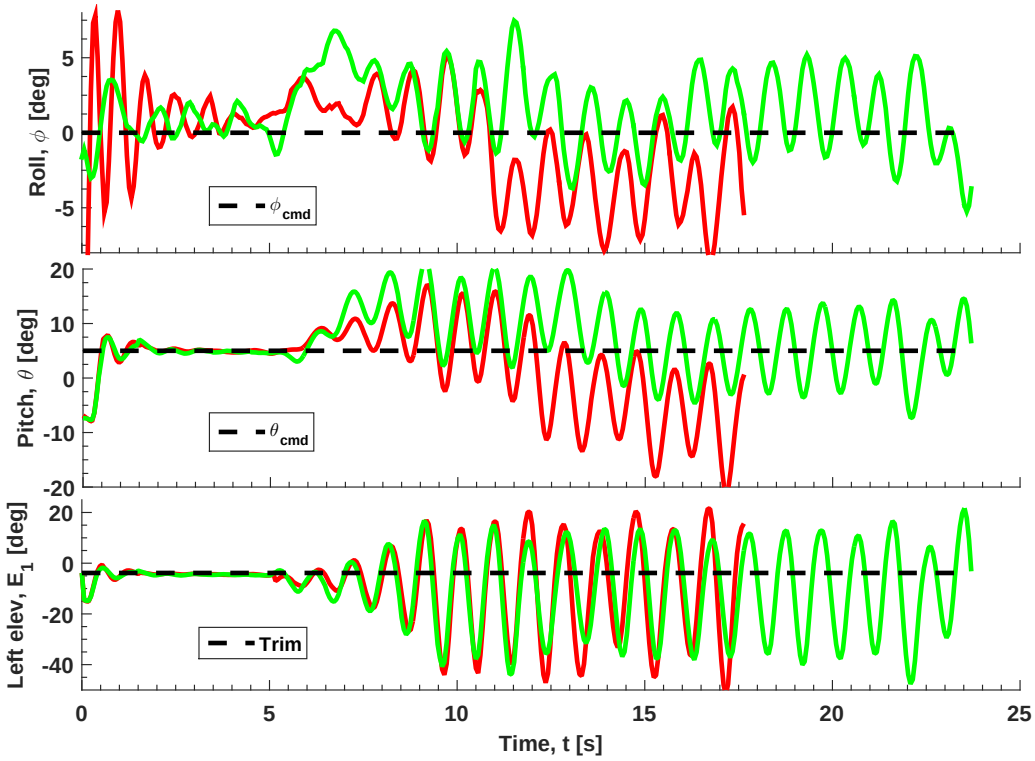

Figure 7. Flight test: H_∞controller: straight and level flight (2 flights)

It is acknowledged that the flight duration is short (approximately 30s), but this is a promising start to more complicated flight tests. In this demonstration, the aircraft directly switches from the pilot's control to fault-tolerant control, without ever switching to baseline control. As a consequence, several runs start with off-nominal initial conditions, leading to worse performance than is actually the case. In a realistic implementation of fault-tolerant control, the aircraft will always switch from baseline control. This should provide initial conditions closer to nominal, leading to better closed loop performance.

IV.B. H_∞flight tests

The flights presented in section IV.A switched directly from the pilot's control to the backup controller. This did not capture the intricacies of switching from the baseline to the backup controller. An attempt is made in this section at a realistic implementation of the fault-tolerant H_∞control law described in section III.C. Specifically, after the pilot engages the autopilot, the aircraft initially starts flying with the baseline controller in the loop. Then, after a preset time delay of 5s, the flight computer is programmed to automatically switch from the baseline to the backup controller. This ensures that all aircraft states have values reasonably close to the nominal initial condition. It is expected that this switching logic should improve the overall performance of the fault-tolerant control. As before, the baseline and backup controllers, and the switching logic are developed using Matlab/Simulink. Subsequently, Simulink Coder is used for automated C code generation.

Figure 7 shows straight and level flight of Baldr, with H_∞control. As before, figure 7 is divided into three subplots, all of which share a common time axis. Each subplot contains data from two different Baldr flights, shown in red and green colors. The longer of the two flights lasted 23s and is shown in green. All other figure notation is the same as before. The time scales of both flights have been shifted such that autopilot engagement starts at $t = 0$s. In the period $t \in [0, 5)$s, the flight computer engages the baseline controller. As seen in the plots, the baseline controller has good command tracking and disturbance rejection properties. At $t = 5$s, the flight computer switches to the backup H_∞controller for the remainder of the flight.

After the backup H_∞controller is engaged ($t > 5$s), oscillations are seen in ϕ, θ, and E_1. These oscillations appear to be undamped: they neither grow nor decay in amplitude. For ϕ, these oscillations have an amplitude of approximately 5° and a mean close to $\phi_{cmd} = 0$. For θ, these oscillations have an amplitude of approximately 7° and a mean close to $\theta_{cmd} = 5°$. Although the presence of these oscillations is not ideal,

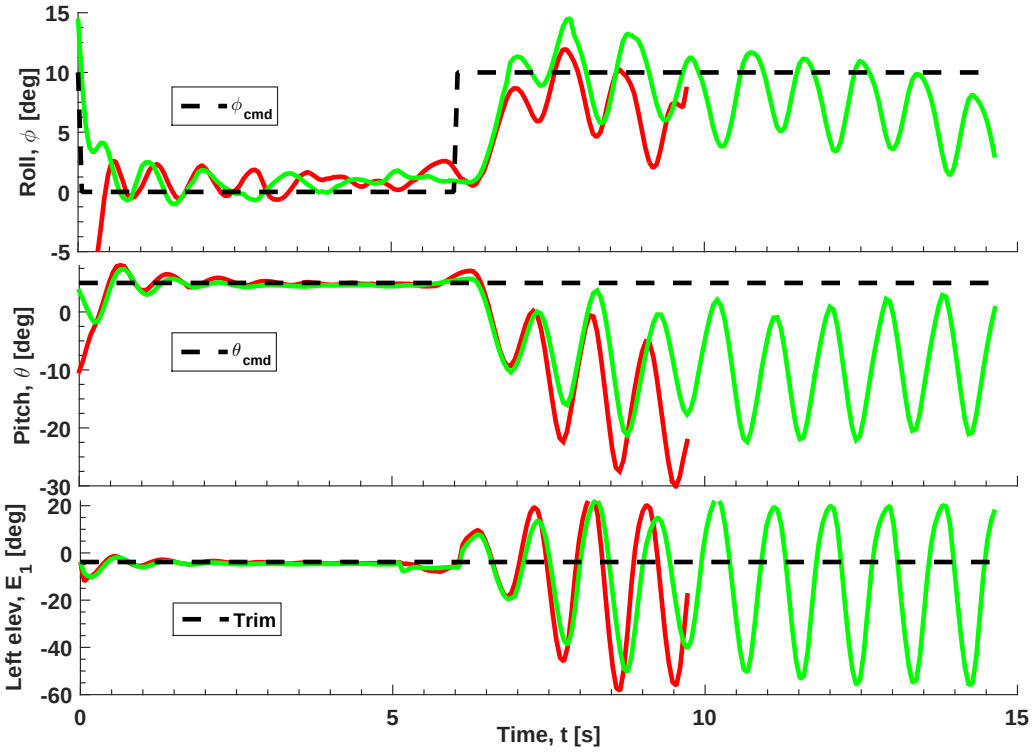

Figure 8. Flight test: H_∞controller: right banked turn (2 flights)

their amplitude is small enough such that there is no real risk of the aircraft experiencing loss-of-control. Specifically, the aircraft remains fully controllable throughout the duration of engagement of the H_∞control law. However, concerning oscillations are seen in the response of E_1. The left elevator command appears to exceed the lower saturation bound of $-25°$, after the H_∞control law is engaged. Despite E_1 exceeding the lower saturation bound, the aircraft states are well behaved. Particularly, both ϕ and θ remain within their respective flight envelope bounds.

The flight test results of Baldr performing right banked turns using H_∞control are shown in figure 8. This figure is organized, and has the same notation, as previous figures. The longer of the two flights lasts 15s and is shown in green. Baldr enters into a right banked turn after a time delay of 6s and stays in this turn for the remainder of the maneuver. The corresponding bank angle command is $+10°$. As before, the flight computer first runs the baseline controller for $t \in [0, 5)$s. At $t = 5$s, the flight computer switches to the H_∞controller. From the ϕ response, it is seen that command tracking is faster with the H_∞controller. The rise time for ϕ is 1s. Oscillations, of similar magnitudes as before, are seen in the ϕ and θ responses. It is concerning that oscillations in θ reach $-30°$. However, the aircraft remains fully controllable and no LOC event occurs. As before, $E1$ appears to exceed the lower saturation bound of $-25°$.

In summary, the H_∞control law allows for Baldr to continue flying even with one control surface. The oscillations seen in figures 7 and 8 can be mitigated by reselecting the weighting functions used in the H_∞synthesis. Specifically, a higher penalty can be imposed on control surface usage by retuning the weight W_{elev} in figure 4. In addition, better weight selection can reduce or avoid the oscillations seen in ϕ, θ, & E_1.

V. Conclusion

This paper introduces the concept of safely flying an aircraft using only one aerodynamic control surface. Two inner-loop controllers were flight tested to perform banked as well as straight and level maneuvers. Both controllers performed satisfactorily in the flight tests. In the best-case scenario, both controllers are able to track roll and pitch reference commands to within five degrees of tolerance. The tracking performance is influenced by atmospheric conditions. This demonstration highlights the potential for applying robust control theory in designing fault-tolerant controllers. In particular, advanced feedback control can be used

to stabilize an aircraft even under extreme fault scenarios, such as a single functional control surface. Future work will involve applying the tools of robust control theory in rigorously analyzing this problem. This analysis will aid in the synthesis of controllers that perform even better.

Appendix

A. Linear aircraft model parameters

The nominal trim point for Baldr is given by the pair $(\bar{x}, \bar{u})$, where $V = 23\mathrm{m\,s^{-1}}$, $\alpha = 5.2°$, $\beta = 0°$, $\phi = 0$, $\theta = 5.2°$, $p = q = r = 0$, $\tau = 0.5$, $E_1 = E_2 = -5.08°$, $R1 = R2 = 0$, $-A1 = A2 = -0.3°$, and $F1 = F2 = 0$. Note that the elevator trim of $-5.08°$ corresponds to the angle of attack of $5.2°$. The aileron trim of $-0.3°$ is used to compensate for the torque from the electric motor. The nonlinear aircraft model is linearized at this nominal trim point. The state-space matrices of the linear model (P) are given in equation 10.

$$P \overset{s}{\coloneqq} \left[\begin{array}{c|c} A & B \\ \hline C & D \end{array}\right] = \left[\begin{array}{cccccccc|c} 0 & 0 & 1 & 0 & 0.09 & 0 & 0 & 0 & 0 \\ 0 & 0 & 0 & 1 & 0 & 0 & 0 & 0 & 0 \\ 0 & 0 & -9.5 & 0.058 & 2.4 & 0.001 & -1.6 & 0 & 8.1 \\ 0 & 0 & 0 & -7.8 & 0.42 & 0.39 & -0.026 & -2.2 & -39 \\ 0 & 0 & 0.58 & -0.26 & -1.7 & 0 & 0.69 & 0 & -0.93 \\ 0 & -9.8 & 0 & -2.1 & 0 & -0.32 & -0.11 & 0.83 & 0.39 \\ 9.8 & 0 & 2.1 & 0 & -23 & 0 & -0.43 & 0 & 0 \\ 0 & -0.89 & 0 & 23 & 0 & -0.33 & -0.096 & -5.7 & -4.6 \\ \hline 1 & 0 & 0 & 0 & 0 & 0 & 0 & 0 & 0 \\ 0 & 1 & 0 & 0 & 0 & 0 & 0 & 0 & 0 \\ 0 & 0 & 1 & 0 & 0 & 0 & 0 & 0 & 0 \\ 0 & 0 & 0 & 1 & 0 & 0 & 0 & 0 & 0 \\ 0 & 0 & 0 & 0 & 1 & 0 & 0 & 0 & 0 \end{array}\right] \tag{10}$$

B. LQG synthesis parameters

The maximum values for the states are defined as: $\phi_{max} = \theta_{max} = 5°$, $p_{max} = q_{max} = r_{max} = 10°\mathrm{s^{-1}}$, and $(u_{max}, v_{max}, w_{max}) = (5, 0.87, 0.44)\,\mathrm{m\,s^{-1}}$. The maximum value for the control surface deflection is defined as: $E_{1,max} = 50°$. The matrices Q and R that appear in equation 9 are defined in equations 11 and 12.

$$Q = diag\left(\phi_{max}^{-2}, \theta_{max}^{-2}, p_{max}^{-2}, q_{max}^{-2}, r_{max}^{-2}, u_{max}^{-2}, v_{max}^{-2}, w_{max}^{-2}\right) \tag{11}$$

$$R = E_{1,max}^{-2} \tag{12}$$

The covariance of the state variables are defined as: $\phi_{cov} = \theta_{cov} = 5 \times 10^{-4}\mathrm{rad^2}$, $p_{cov} = q_{cov} = r_{cov} = 5 \times 10^{-5}\mathrm{rad^2 s^{-2}}$, $u_{cov} = v_{cov} = w_{cov} = 0.05\mathrm{m^2/s^2}$. The covariance of the process noise (w) and measurement noise (v) signals are defined in equations 13 and 14.

$$E\left[ww^T\right] = diag\left(\phi_{cov}, \theta_{cov}, p_{cov}, q_{cov}, r_{cov}, u_{cov}, v_{cov}, w_{cov}\right) \tag{13}$$

$$E\left[vv^T\right] = diag\left(\phi_{cov}, \theta_{cov}, p_{cov}, q_{cov}, r_{cov}\right) \tag{14}$$

The integral gains used for command tracking are -8 in the ϕ channel and -6 in the θ channel.

C. H_∞synthesis parameters

The weighting functions for the H_∞synthesis are listed in table 2.

Acknowledgments

The authors would like to thank Brian Taylor, Chris Regan, Danny Chryst, and Karen Hamidun for providing support with the flight tests. The authors acknowledge the members of the senior design team

Table 2. Weighting functions used in H_∞ synthesis

Weight	Transfer function
P_ϕ	$\frac{0.1s+5.973}{s+0.176}$
P_θ	$\frac{0.1s+12.03}{s+6.766}$
$P_{p,q,r}$	$diag\,(5.73, 5.73, 5.73)$
$N_{p,q,r}$	$diag\,(0.1, 0.1, 0.1)$
D_{elev}	0.01
W_{elev}	$\frac{1.423s+76.31}{s+119.2}$
ACT	$\frac{50.27}{s+50.27}$

that performed the reliability analysis for the Ultra Stick 120: Jeremy Amos, Erik Bergquist, Jay Cole, Justin Phillips, Shawn Reimann, and Simon Shuster. This work was supported by the National Science Foundation under Grant No. NSF/CNS-1329390 entitled "CPS: Breakthrough: Collaborative Research: Managing Uncertainty in the Design of Safety-Critical Aviation Systems". Any opinions, findings, and conclusions or recommendations expressed in this paper are those of the authors and do not necessarily reflect the views of the NSF.

References

[1]United States Congress, "House Resolution 658: FAA Modernization and Reform Act of 2012," 2012, Section 332: Integration of Civil Unmanned Aircraft Systems into National Airspace System.

[2]Federal Aviation Administration, "Notice of Proposed Rulemaking," February 2015.

[3]Yeh, Y. C., "Triple-triple redundant 777 primary flight computer," *Proceedings of the 1996 IEEE Aerospace Applications Conference*, Aspen, CO, USA, 1996, pp. 293–307.

[4]University of Minnesota, "UAV Research Group," `www.uav.aem.umn.edu`, 2014.

[5]Amos, J., Bergquist, E., Cole, J., Phillips, J., Reimann, S., and Shuster, S., "UAV for Reliability," `www.aem.umn.edu/∼SeilerControl/SafetyCritical.shtml`, December 2013.

[6]Sentera, `www.sentera.com`.

[7]Agribotix, `www.agribotix.com/hornet-drone-system`.

[8]Trimble, `www.uas.trimble.com/ux5`.

[9]senseFly, `www.sensefly.com/drones/ebee.html`.

[10]Murch, A. M., Paw, Y. C., Pandita, R., Li, Z., and Balas, G., "A Low Cost Small UAV Flight Research Facility," *Advances in Aerospace Guidance, Navigation and Control*, edited by F. Holzapfel and S. Theil, Springer-Verlag Berlin Heidelberg, 2011, pp. 29–40.

[11]Dorobantu, A., Johnson, W., Lie, F. A., Taylor, B., Murch, A., Paw, Y. C., Gebre-Egziabher, D., and Balas, G., "An Airborne Experimental Test Platform: From Theory to Flight," *American Control Conference*, June 2013, pp. 659–673.

[12]Lie, F. A., Dorbantu, A., Taylor, B., Gebre-Egziabher, D., Seiler, P., and Balas, G., "An Airborne Experimental Test Platform: From Theory to Flight (Part 1)," *InsideGNSS*, April 2014, pp. 44–58.

[13]Stevens, B. L. and Lewis, F. L., *Aircraft Control and Simulation*, John Wiley & Sons, 1992.

[14]Hoe, G., Owens, D., and Denham, C., "Forced Oscillation Wind Tunnel Testing for FASER Flight Research Aircraft," *AIAA AFM Conference*, 2012.

[15]Owens, D., Cox, D. E., and Morelli, E. A., "Development of a Low-Cost Sub-Scale Aircraft for Flight Research: The FASER Project," *25th AIAA Aerodynamic Measurement Technology and Ground Testing Conference*, 2006.

[16]Venkataraman, R. and Seiler, P., "Model-Based Detection and Isolation of Rudder Faults for a Small UAS," *AIAA Guidance, Navigation, and Control Conference*, 2015.

[17]Chen, J. and Patton, R., *Robust Model-Based Fault Diagnosis for Dynamic Systems*, Kluwer, Boston, MA, 1999.

[18]Ding, S. X., *Model-Based Fault Diagnosis Techniques: Design Schemes, Algorithms, and Tools*, Springer-Verlag, Germany, 1st ed., 2008.

[19]Gertler, J. J., *Fault detection and diagnosis in engineering systems*, Marcel Dekker, 1st ed., 1998.

[20]Cook, M. V., *Flight Dynamics Principles*, Elsevier, 2nd ed., 2007.

[21]Skogestad, S. and Postlethwaite, I., *Multivariable Feedback Control: Analysis and Design*, Wiley, 2005.

[22]Dorobantu, A., Murch, A. M., and Balas, G. J., "H_∞ Robust Control Design for the NASA AirSTAR Flight Test Vehicle," *50th AIAA Aerospace Sciences Meeting*, 2012.